IN THE NAME OF ALLAH,
THE MOST GRACIOUS,
THE MOST MERCIFUL

Kingdom of Saudi Arabia
Ministry of Education
Majmaah University

جامعة المجمعة
Majmaah University

JEAS

JOURNAL OF ENGINEERING AND APPLIED SCIENCES

A Refereed Academic Journal Published by the
Publishing and Translation Center at Majmaah Universtiy

Vol. 2, Issue (1) November, 2015 ISSN: 1658 - 6638

Publishing & Translation Center - MU

About the Journal

Journal of Engineering and Applied Sciences (JEAS)

Vision

Pioneer journal in the publication of advanced research in engineering and applied sciences.

Mission

A peer-review process which is transparent and rigorous

Objectives

a) Support research that addresses current problems facing humanity.

b) Provide an avenue for exchange of research interests and facilitate the communication among researchers.

Scope

JEAS accepts articles in the field of engineering and applied sciences. Engineering areas covered by JEAS include:

- Mechanical Engineering
- Civil Engineering
- Industrial Engineering
- Electrical Engineering
- Environmental Engineering
- Chemical Engineering
- Architectural Engineering

Areas under applied sciences include:

- Biological Science
- Environmental Science
- Biotechnology
- Biomathematics
- Applied Mathematics
- Applied Physics
- Earth Science

Correspondence and Subscription

Majmaah University, Post Box 66, AlMajmaah 11952, KSA

email: jeas@mu.edu.sa

Journal of Engineering and Applied Sciences

Editorial

Scientific publishing has brought many challenges to authors. With increasing number of scientific journals, varying scopes and reviewing requirements, and cost of publishing to authors, finding the right journal to publish an article is a decision many authors must bitterly confront and resolve. The publication of scientific findings is an integral part of the life of researchers; and the process of publishing has evolved to become an efficient system of decimating knowledge and collaboration among scientists. Science journals have institutionalized procedures to manage large volume of article submissions per year; in many cases, journals began to define narrower scopes for a dual purpose: managing submissions and delivering outstanding research.

Based on recent studies, the scientific publishing world consists of more than 25 thousands active journals in various disciplines and fields. ScienceDirect hosts 3,348 journals (as of February 2014). The Directory of Open Access Journals lists in its search engine more than 9,800 open access online journals.

According to recent estimates, the number of scientific journals grows by 3% per year worldwide. With this large number of journals, journals may find it harder to stay afloat.

In its inauguration, the board ofeditors is honored to introduce to the scientific community the Journal of Engineering and Applied Sciences - JEAS, another scientific journal from Majmaah University. The board has pledged a commitment to JEAS authors and readers to bringing the most dynamic and vibrant journal management with ever quest for better satisfaction.

Dr Muhammad Al-Salamah

Contents

Effects of UV Radiation and Isothermal Crystallization on LDPE/ MMT Nanocomposites

Samir Al-Zobaidi
Department of Physics, College of Science, Majmaah University, Al-Zulfi, 11932, Saudi Arabia, s.alzobaidi@mu.edu.sa

Abstract

In order to understand the effect of both UV radiation and isothermal crystallization temperature on LDPE/MMT nanocomposites we used one composition of LDPE/MMT nanocomposites. All samples were crystallized isothermally at two selected temperatures of 100 and 104oC for a fixed time of 5h. The crystallization temperature was chosen to be above the non-isothermal crystallization of LDPE/MMT nanocomposites. XRD showed that the material used consisted of two stable monoclinic and orthorhombic phases. Both phases have shown different respond to the crystallization process. Intercalation of clay was also affected by the crystallization temperatures and UV exposure. Results obtained from XRD, DSC and FTIR were in agreement with each other. A third phase that is thermally less stable was also observed, its thermal respond was larger since it contains low molecular weight entities which makes it more vulnerable to any UV exposure.

Keywords: LDPE; montmorillonite;isothermal, crystallization; UV irradiation, nanocomposites.

Article history: Received: July 12, 2015, Accepted: January 26, 2016

1. Introduction:

The most common layered silicates used in preparing polymer/layered silicate nanocomposites are Montmorillonite (MMT). It is one of the typical natural minerals in the smectite clay family. The stacked layers of MMT are of about 1 nm in thickness and are separated from each other by a weak dipolar force. They form interlayers or galleries that are usually occupied by exchangeable Na^{+}, K^{+}, Ca^{+2} and Mg^{+2} cations. In order to improve the ion exchangeability of the layered silicates, MMT is usually modified organically by exchanging the alkali counter ions with cationic-organic surfactans, such as alkylammoniums [1, 2].

The organic modification of MMT allows the polymer molecules to intercalate within the galleries. Depending on the strength of the interfacial interactions between the polymer matrix and layered silicates, polymer/layered silicate can form either intercalated nanocomposites, where few molecular layers of polymer are intercalated, or exfoliated nanocomposites where the individual clay layers are separated in a continuous polymer matrix by an average distances that depends on the clay loadings [3]. Well exfoliated nano-

composites show better mechanical properties compared to its pure polymer. However, the interfacial interaction between LDPE and MMT is generally weak and require an intermediate agent like Maleic anhydride.

The importance of LDPE in the different fields of industry is well-known. Based on recent statistics [4], 17.5% of the total consumption of plastic industries in Europe is of LDPE. Its applications vary from food packaging and shopping bags to electrical applications, auto parts, construction sites, and many other important and crucial applications. LDPE/layered silicates composites have shown improvement in their mechanical properties, flame retarding and thermal stability.

The isothermal crystallization of LDPE and some of its blends was studied thoroughly in literature [5-10]. Effect of radiation on the properties of LDPE and LDPE/MMT nano-composites has also been extensively studied in literature. High energy ion beam irradiation [11-13], γ radiation [14-16] and electron beam irradiation [17-19] are examples to the methods used to affect the molecular structure of certain polymers, including LDPE, and hence study its influence on the properties of these polymers. Photo-oxidation using UV irradiation has also gained wide interest in literature [20, 21]. Studying the rheological behavior of LDPE at temperatures exceeding their melting temperature and under UV irradiation was the goal of *Marek* and *Verney* [22] where they concluded that LDPE has shown less chain-cession compared to HDPE and PP. On the other hand, UV irradiation of LDPE/montmorillonite nano-composites did not gain similar attentiveness in literature. Sánchez-Valdés *et. al*. [23] studied the effect of photo-oxidation on two groups of LDPE/ clay nano-composites where they concluded that clay has enhanced the degradation rate of the nano- composites compared to the raw PE material.

In this study we irradiated an arbitrary selected composition of LDPE/MMT composite using short wavelength UV source. UV irradiation was conducted at two different isothermal crystallization temperatures in order to investigate its effect on the molecular and crystalline structure of these composites.

2. Experimental procedure:

2.1. Materials

The raw material of low density polyethylene (LDPE) used in this study is a commercial grade produced by SABIC (HP4023W) company. The melt flow rate of this product is4.0 g/10min. according to ASTM D1238. The nano-clay nanomer 1.44P is a montmorillonite clay surface modified with 35-45 wt. % dimethyl dialkyl (C14-C18) amine and is a product of Sigma Aldrich. The Maleic Anhydride grafted polyethylene (MA-g-PE) is used as a compatibilizer and is also a product of Sigma Aldrich.

2.2 *Sample preparation*:

A mixture of 93 wt. % of LDPE, 3 wt. % of MA-g-PE and 4 wt. % of nano-clay was prepared by melt mixing it using Dynisco laboratory mixer. The barrel temperature was

set at 140°C, while the orifice temperature was set at 130°C. The homogeneous compound was quenched in water at room temperature. The compound was then slightly pressed at 140°C using Carver hot press to form homogeneous films of a thickness of about 0.1 mm.

Samples were divided into two main groups based on the method of UV treatment. A short UV wavelength of 254 nm at a distance of 13 cm was used for all samples as summarized in table 1.

Table 1 List of the nomenclature of the samples used.

Composite's symbol	UV treatment method	T_c (°C)
A100	Samples were exposed to UV radiation for 5 hours during the isothermal crystallization process.	100
A104		104
D100	Samples were not exposed to any UV radiation.	100
D104		104

Using Linkam T95-HS hot stage, the heating profile used to crystallize the samples was as follow: melting at 130°C for 10 minutes to remove any thermal history; then rapidly cooling down to an arbitrary selected crystallization temperature of T_c = 100°C or 104°C; annealing for 5 hours to allow sufficient time for complete crystallization.

2.3 *Testing methods:*

Wide angle x-ray diffraction patterns were obtained by using BrukerD8 advance X-ray diffractometer with Cu K_α radiation of wavelength λ = 0.154 nm, a running voltage of 40.0 (kV) and a current of40.0 (mA).

DSC endotherms were taken using Perkin Elmer DSC 8000. All samples were heated at the rate of 10°C/min, then cooled down to room temperature at the same rate.

FTIR spectra were taken for all samples using Nicolet iS5 FTIR spectrometer in the mid-IR range (400 – 4000 cm^{-1}) at a resolution of 2 cm^{-1}.

3. Data and results:

The single broad endotherm peak, appearsin the melting behavior of raw LDPE material see Fig. 1, indicates a relatively wide molecular weight distribution with a melting peak of 109.4°C. Two second order transitions at around 59°C and 73°C are observed. The two second order transitions are believed to be due to the presence of the slip and anti-block additives that were added to the raw material, as specified in the data sheet of LDPE raw material.

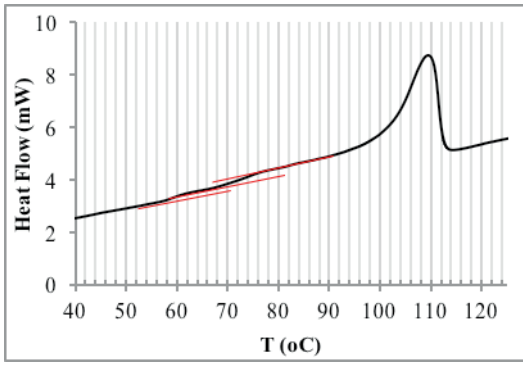

Fig. 1: DSC endotherm of raw LDPE

The melting behavior of sample D is shown in Fig. 2. As can be observed, its melting behavior differs significantly with changing the isothermal crystallization temperature. Three distinct peaks have appeared for both

crystallization temperatures. All samples show three distinct peaks. At lower temperature, in the range of 96.0°C, a broad melting peak with small heat flow appears; while a peak with smaller FWHM and higher heat flow values appears in the range of 106.0°C. At around 109.5°C a third peak that is sharper and has larger heat flow values appears. This melting point coincides with that of the raw material, which suggests that at this temperature similar crystalline phases have melted. The absence of the multi-peak behavior of the raw material (Fig. 1) suggests that the addition of MMT and PE-*g*-MA is the reason behind this action.

The multi-peak behavior in DSC thermographs could be attributed to either the presence of different crystalline structures or to the different molecular weight population. In this work it is believed that both interpretations are valid. The small and broad peak at lower temperature is believed to be due to the melting of crystals that were formed by relatively low molecular weight chains [24]. These chains start to segregate producing some form of organized entities during the cooling process from melting to the crystallization temperature [25].

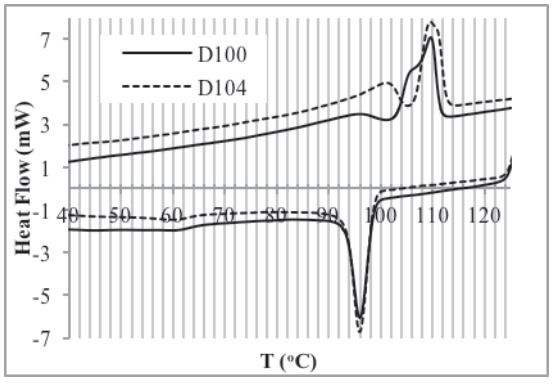

Fig. 2: DSC thermographs of sample D crystallized at 100 and 104°C.

The other two larger peaks are believed to be due to the formation of two different crystalline phases: the monoclinic and orthorhombic phases [26]. As will be discussed later, peak 2 is believed to refer to the melting of the monoclinic phase while peak 3 represents the melting of the orthorhombic phase. Similar argument can be suggested for sample A 100 as illustrated in Fig. 3.

On the other hand, although samples A and D that were crystallized at 104°C have shown similar multi-peak behavior, the positions of these peaks have changed towards larger temperatures. Peak 1 has shifted to the range of 100°C, which suggests that the small entities crystallized during the cooling process managed to grow more, forming extended crystalline entities and hence larger melting temperatures.

Peak 2 has shifted 4-5°C towards larger temperatures to about 111°C. It is believed that annealing the composite at lower super-cooling temperatures allowed the chains of the monoclinic crystals to extend more due to the larger chain mobility at higher temperatures. Peak 3 however, did not change its position. Apparently orthorhombic crystals are very stable and did not show any respond to the change in crystallization temperature. This observation contradicts with what is reported in literature where larger crystallization temperatures yielded larger melting points [27-29]. This contradiction could be justified by assuming that the orthorhombic crystals are formed by the longer molecular chains. It is possible that the branches of these molecules hinder any additional growth of the orthorhombic crystals.

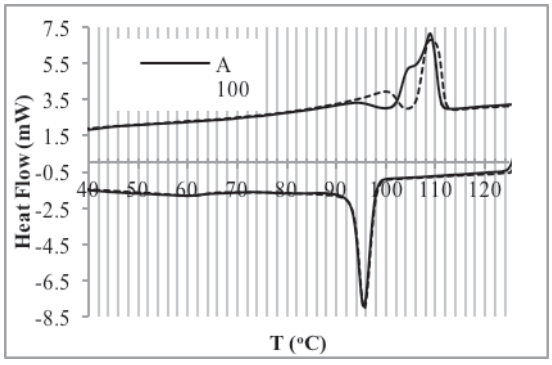

Fig. 3: DSC endotherms and exotherms of sample A crystallized at 100 and 104 °C.

Crystals formed in the monoclinic phase, however, have the ability to include these branches in the crystalline phase which, consequently, allow for the extension of chains in the crystalline phase, and hence requires larger heat energy to melt it.

By comparing the melting temperatures of samples A and D, listed in Table 2, it can be noticed that sample D is more thermally stable than sample A. This can be noticed from the larger values of the melting and crystallization peaks of sample D100 compared to A100 and D104 compared to A104. This behavior is expected since sample D was not exposed to UV radiation hence no chain-cessions have occurred.

The UV exposure of sample A during the crystallization process is responsible for reducing its thermal stability. It is suggested that during the crystallization process free radicals are generated. Such free radicals are responsible for chain-cession especially for small molecular chains as suggested by the temperature difference of peak 1. Peak 3, in general, has shown less respond to UV exposure. In conclusion, the exposing method used for sample A has significant effect only on both monoclinic phase and the low molecular weight population. Further studies are required to understand the time effect of UV exposure on the thermal stability of these phases.

Table 2 List of the peak positions obtained from DSC thermographs.

Composite's symbol	T_m(°C) peak 1	T_m(°C) peak 2	T_m(°C) peak 3	T_C(°C) peak
Raw material	--	--	109.38	94.55
A100	92.94	104.54	109.39	95.73
A104	99.71	110.32	108.86	95.51
D100	95.05	105.51	109.71	96.16
D104	101.00	110.96	109.70	96.12

XRD results shown in Fig.4 and Fig. 5 coincide with what was suggested by DSC. The two (110) and (200) orthorhombic peaks appear at angles $2\theta \approx 21.7^o$ and 24.0^o respectively, while the monoclinic (010) appears at $2\theta \approx 19.6^o$ [30]. The appearance of both crystalline phases could not be referred to the addition of MMT or MA since these phases appear in the diffraction of raw material too (Fig. 4). However, the two peaks formed at lower scattering angles $2\theta \approx 2.5^o$ and 4.9^o are referred to the addition of MMT clay in which intercalated nano-composites are formed [31]. Comparing XRD results with DSC thermal behavior we can conclude that the endotherm peaks formed at larger temperatures (~ 109.5°C) in Figs. 2 and 3 are due to the melting of the orthorhombic

crystals while those formed at temperature near 104°C represent the melting of the monoclinic crystals.

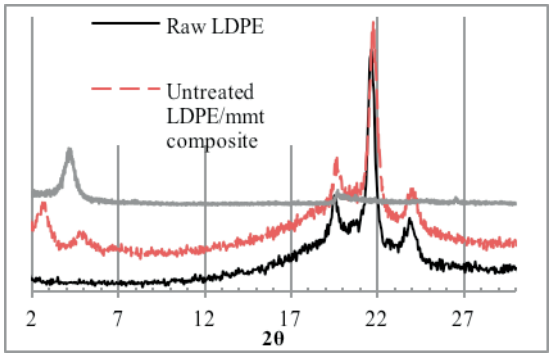

Fig. 4: X-ray diffractions of raw LDPE, LDPE composite without treatment and clay.

XRD spectra of samples A100 and D100 shown in Fig. 5 did not show any change in the type or size of crystals formed. This could be concluded from the absence of any new peaks or any shift in the peak positions. The fact that the d_{001} and d_{002} spacing of the silicate layers is larger for sample D, as listed in Table 3, induces that UV exposure jeopardizes the intercalation process. Free radicals are possibly interacting with the anions and cations in between the layered silicates causing its intermolecular spacing to decrease.

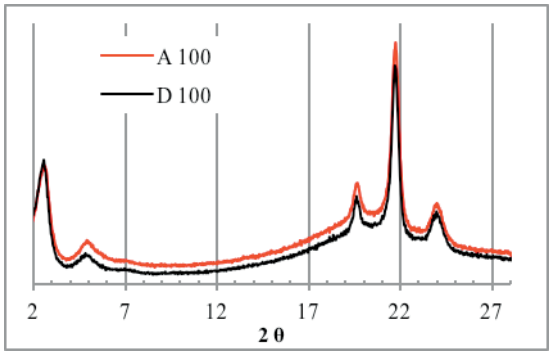

Fig. 5: X-ray diffractions of samples crystalized at 100 °C

Table 3 List of *d* spacings of the two peaks generated due to the existance of MMT

Sample	2θ	d_{001} (Å)	2θ	d_{002} (Å)
A100	2.53	34.852	4.93	17.923
A104	2.48	35.595	5.00.	17.674
D100	2.49	35.512	4.86	18.164
D104	2.47	35.736	4.78	18.480

Another possible interpretation to these results is that the molecules of maleic anhydride are largely affected by free radicals causing some chain-cession to occur. This will eventually affect the compatibility between the clay and polymer hence causing some of LDPE chains to be expelled from in between the layered silicates. This observation is in agreement with the depression of the non-isothermal crystallization temperature listed in Table 2.

FTIR spectra shown in Fig. 6 represent those of the three reference materials: MMT, raw LDPE and the untreated LDPE/MMT composite. The spectra were taken for a full range of 400-4000 cm^{-1}, however, our focus will be on the limited range of 700-1500 cm^{-1}. The importance of this range comes from the fact that it includes both the rocking CH_2 mode (700-740 cm^{-1}) and the bending CH_2 mode (700-740 cm^{-1}).

The rocking CH_2 mode of samples A100 and D100 are illustrated in Fig. 7, where the left side peaks at 719 cm^{-1} represent the ordered chains of the monoclinic phase and the right side peaks at 730 cm^{-1} refer to the orthorhombic crystalline structure [32]. The relative intensities of these two peaks are

comparable for A100, while D100 shows a dominating monoclinic phase. At an isothermal crystallization temperature of T_c = 104°C (Fig. 8) more rocking mode chains are formed in the monoclinic phase. The equivalent intensities of sample A100 (Fig. 7) could be referred to the UV exposure of the sample, where more of the rocking mode chains are crystallizing in the orthorhombic phase.

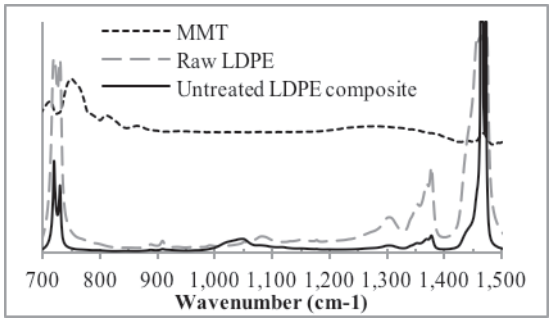

Fig. 6: FTIR spectra of rawLDPE, MMT and an untreated composite

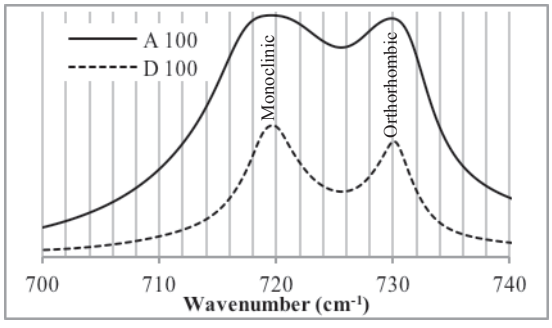

Fig. 7 : FTIR spectra of A100 and D100 in the rocking mode

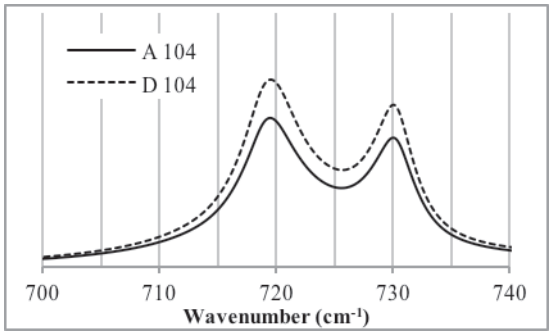

Figure 8: FTIR spectra of A104 and D104 in the rocking mode

The absorption spectra of the bending mode of methylene groups are illustrated in Figs. 9 and 10. Bands in the (1461-1463 cm^{-1}) region represent the absorption of the all *trans* orthorhombic chains, while the (1466-1467 cm^{-1}) region represents the all *trans* amorphous molecules. The 1472 cm^{-1}, however, is believed to represent the dominating phase of monoclinic crystals. The broad spectrum of A100 in Fig. 9 is due to the large thickness of the sample used hence cannot be included in this discussion.

Generally, the relative intensity $I_{Mon.}/I_{Orth.}$ of the bending mode is larger than that of the rocking mode for all samples studied. This explains the dependency of the melting temperature of monoclinic phase on the isothermal crystallization temperature and UV exposure.

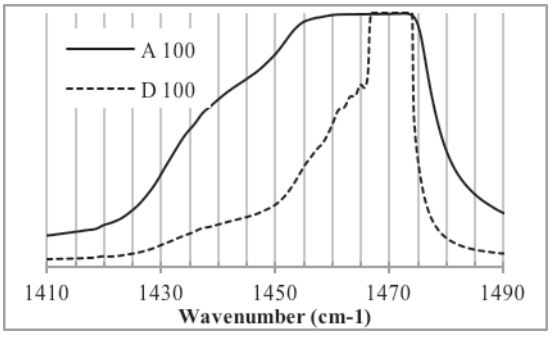

Fig. 9: FTIR spectra of A100 and D100 in the bending mode

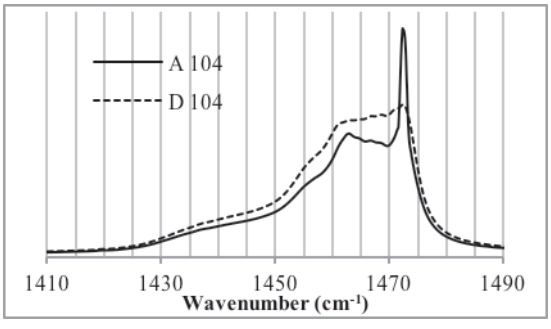

Fig. 10: FTIR spectra of A104 and D104 in the bending mode

An exception to this discussion could be made for sample D104, where its $I_{Mon.}/I_{Orth}$ is close to unity. The less domination of the monoclinic phase and the obvious presence of the amorphous phase, in addition to the fact that this sample has the largest d_{001} silicate spacing as listed in Table 1, suggest that an additional monoclinic chains might have been intercalated in between the layered silicates hence its bending vibration was hindered due to the smaller degree of freedom. Accordingly, it can be suggested that for better intercalation process samples should be isothermally crystalized at lower super cooling temperatures. In order to confirm this assumption further studies are required.

4. Conclusion:

In this study we tried to study the effect of both isothermal crystallization temperature and UV exposure on the behavior of LDPE/MMT nano-composites and hence their effect on the properties of these composites. By varying the two parameters we attempted to obtain the optimum conditions for the intercalation process; and consequently optimize the mechanical properties of these nano-composites.

XRD results showed that the nano-composites compose of two stable crystalline structures, orthorhombic and monoclinic, in addition to a third phase of crystalline small chain entities. UV exposure has less effect on the thermal stability of LDPE/MMT nano-composites compared to the effect of isothermal crystallization temperatures. The monoclinic crystalline structure has responded more effectually to the change of crystallization conditions compared to the orthorhombic structure.

Chains growing in the monoclinic phase allow the small branches of LDPE to be included in the crystalline phase hence extending the molecular chains of the crystalline phase. In contrast, orthorhombic crystals showed no sign of chain extension and, consequently, no sign of branch inclusion.

Intercalation process was affected by the method of UV exposure. UV radiation jeopardized the intercalation process. However, a sign of better intercalation is observed at larger isothermal crystallization temperature.

Acknowledgments

This work has been funded by the deanship of scientific research at Majmaah University under grant number 16. The help and support of the dean of scientific research and the head of Physics Department Dr. Thamer Alharbi is greatly appreciable. All measurements were done in our Materials Science Research Lab.

References

[1] Qin, H., Zhang, S., Liu, H., Xie, S., Yang, M., Shen, D., 2005. Photo-oxidative degradation of polypropylene/montmorillonite nanocomposites. Polymer46(9), pp 3149–3156.

[2]Manias, E., Touny, A., Wu, L., Strawhecker, K., Lu, B., Chung, C., 2001.Polypropylene/Montmorillonite Nanocomposites. Review of the Synthetic Routes and Materials Properties. Chemistry of Material13, pp 3516-3523.

[3] Gerald, S., 1990. Polymers with enhanced photodegradability. Journal of Photochemistry and

Photobiology A: Chemistry 51(1), pp 73–79.

[4] http://www.plasticseurope.org/plastics-industry/market-and-economics.aspx

[5]Li, J., Shanks, R.A. and Long, Y., 2001. Isothermal crystallization and spherulite structure of partially miscible polypropylene–linear low-density polyethylene blends.Journal of applied polymer science82(3), pp.628-639.

[6]Martuscelli, E., Pracella, M., Volpe, G.D. and Greco, P., 1984. Morphology, crystallization, and thermal behaviour of isotactic polypropylene/low density polyethylene blends.Die Makromolekulare Chemie185(5), pp.1041-1061.

[7]Schouterden, P., Groeninckx, G., Van der Heijden, B. and Jansen, F., 1987. Fractionation and thermal behaviour of linear low density polyethylene. Polymer28(12), pp.2099-2104.

[8]Janigová, I., Chodák, I. and Chorváth, I., 1992. The influence of crosslinking on isothermal crystallization of LDPE filled with silica.European polymer journal28(12), pp.1547-1552.

[9]Grady, B.P., Genetti, W.B., Lamirand, R.J. and Shah, M., 2001. An investigation of heat transfer effects in isothermal crystallization studies of low-density polyethylene.Polymer Engineering & Science41(5), pp.820-829.

[10]Hargis, M.J. and Grady, B.P., 2006. Effect of sample size on isothermal crystallization measurements performed in a differential scanning calorimeter: A method to determine avrami parameters without sample thickness effects.Thermochimica acta443(2), pp.147-158.

[11] Dhillon, R., K., Singh, P., Gupta, S., K., Singh, S., Kumar, R., 2013. Study of high energy (MeV) N^{6+}ion and gamma radiation induced modifications in low density polyethylene (LDPE) polymer.Nuclear Instruments and Methods in Physics Research Section B: Beam Interactions with Materials and Atoms301, pp 12–16.

[12] Singh, R., Samra, K., S., Kumar, R., Singh, L., 2008. Proton (3MeV) and copper (120MeV) ion irradiation effects in low-density polyethylene (LDPE).Radiation Physics and Chemistry77(1), pp 53–57.

[13] Vinodh, Kumar, S., Ghadei, B., Krishna, J., B., M., Bhattacharya, S., C., Saha, A., 2009. High-energy C+ ion-irradiated low-density polyethylene (LDPE): Spectroscopic and morphological investigation. Radiation Physics and Chemistry78(5), pp 351–355.

[14] Zhang, J., Rahman, A., Z., M., S., Li, Y., Yang, J., Wu, Y., Yuan, D., Wang, B., 2015. Radiation induced modifications on structural and luminescence properties of LDPE–Na_2SO_4:Sm^{3+} composites by γ-ray.Optical Materials 42, pp 251–255.

[15] Moez, A., A., Aly, S., S., Elshaer, Y., H., 2012. Effect of gamma radiation on low density polyethylene (LDPE) films: optical, dielectric and FTIR studies.Spectrochimica Acta. Part A, Molecular and Biomolecular Spectroscopy 93, pp 203–207.

[16] Alvarez, V., A., Perez, C., J., 2013. Gamma irradiated LDPE in presence of oxygen. Part I. Non-isothermal crystallization.Thermochimica Acta 570, pp 64–73.

[17] Han, J., Castell-Perez, M., E., Moreira, R., G., 2007. The influence of electron beam irradiation of antimicrobial-coated LDPE/polyamide films on antimicrobial activity and film properties.LWT - Food Science and Technology 40(9),pp 1545–1554.

[18] Sabet, M., Hassan, A., Ratnam, C., T., 2012. Electron beam irradiation of low density polyethylene/ethylene vinyl acetate filled with metal hydroxides for wire and cable applications.Polymer Degradation and Stability 97(8),pp 1432–1437.

[19] Soltani, Z., Ziaie, F., Ghaffari, M., Afarideh, H., Ehsani, M., 2013. Mechanical and thermal properties and morphological studies of 10MeV electron beam irradiated LDPE/hydroxyapatite nano-composite. Radiation Physics and Chemistry83,pp 79–85.

[20] Dintcheva, N., T., Alessi, S., Arrigo, R., Przybytniak, G., Spadaro, G., 2012. Influence of the e-beam irradiation and photo-oxidation aging on the structure and properties of LDPE-OMMT nanocomposite films.Radiation Physics and Chemistry 81(4), pp 432–436.

[21] Giesse, R., De Paoli, M.-A., 1988. Surface and bulk oxidation of low-density polyethylene under UV-irradiation.*Polymer Degradation and Stability*

21(2), pp 181–187.

[22] Marek, A., A., Verney, V., 2015. Rheological behavior of polyolefins during UV irradiation at high temperature as a coupled degradative process. European Polymer Journal 72, pp 1–11.

[23] Sánchez-Valdés, S., Martínez, Colunga, J., G., López-Quintanilla, M., L., Yañez, Flores, I., García-Salazar, M., L., González, Cantu, C., 2008. Preparation and UV weathering of polyethylene nanocomposites.Polymer Bulletin 60(6), pp 829–836.

[24] Maxwell, A., S., A., P., Unwin, I., M., Ward, MI, Abo El Maaty, M., M., Shahin, R., H., Olley, D., C., Bassett, 1997. The effect of molecular weight on the deformation behaviour of pressure annealed polyethylene.Journal of materials science32(3), pp 567-574.

[25] Kim, M., H., Phillips, P., J., 1998. Nonisothermal melting and crystallization studies of homogeneous ethylene/α-olefin random copolymers.Journal of applied polymer science70(10), pp 1893-1905.

[26] Vanden, Eynde, S., Sanjay, Rastogi, V., B., F., Mathot, Harry, Reynaers, 2000. Ethylene-1-octene copolymers at elevated pressure-temperature. 1. Order-disorder transition.Macromolecules33(26), pp 9696-9704.

[27]Shi, X., Jin, J., Chen, S. and Zhang, J., 2009. Multiple melting and partial miscibility of ethylene-vinyl acetate copolymer/low density polyethylene blends.Journal of applied polymer science113(5), pp.2863-2871.

[28]Wang, C., Chu, M.C., Lin, T.L., Lai, S.M., Shih, H.H. and Yang, J.C., 2001. Microstructures of a highly short-chain branched polyethylene. Polymer42(4), pp.1733-1741.

[29]Dimeska, A. and Phillips, P.J., 2006. High pressure crystallization of random propylene–ethylene copolymers: α–γ Phase diagram.Polymer*47*(15), pp.5445-5456.

[30] Vanden, Eynde, S., Rastogi, S., Mathot, V., B., F., Reynaers, H., 2000. Ethylene-1-octene copolymers at elevated pressure-temperature. 1. Order-disorder transition.Macromolecules33(26), pp 9696-9704.

[31] Liu, S.-P., Tu, L.-C., 2011. Studies on mechanical properties of dispersing intercalated silane montmorillonite in low density polyethylene matrix. International Communications in Heat and Mass Transfer38(7), pp 879–886.

[32]Pilar, T., Julio, G., Rafael, S., Mario, H., Nuria, G., 2009. Evidence of a monoclinic-like amorphous phase in composites of LDPE with spherical, fibrous and laminar nanofillers as studied by infrared spectroscopy.European Polymer Journal45, pp 30–39.

Microstructural and Thermal Properties of Porous Aluminum Filled with Nanocrystalline Silicon

Taher Ghrib*
Laboratory of Physical Alloys (LPA), Faculty of Science of Dammam, University of Dammam, Saudi Arabia,
taher.ghrib@yahoo.fr.

Amal Lafy Al-Otaibi
Laboratory of Physical Alloys (LPA), Faculty of Science of Dammam, University of Dammam, Saudi Arabia,
amalotiaibi@uod.edu.sa.

Munirah Abdullah Almessiere
Laboratory of Physical Alloys (LPA), Faculty of Science of Dammam, University of Dammam, Saudi Arabia,
malmessiere@uod.edu.sa.

Abstract

In this work, the structural, thermal and optical properties of porous aluminum thin film carried out with various intensities of the anodization current in sulfuric acid. The obtained pores at the surface are filled by nanocrystalline silicon (nc-Si) thin films deposited by plasma enhancement chemical vapor deposition (PECVD), which the role is to improving its optical absorption and thermal properties. The prepared sample is an assembly of three different media such as Al sample/ Porous aluminum layer filled with silicon (PAS)/ nanocrystallite silicon layer (nc-Si). The effect of anodization current on the microstructure of porous aluminium and the effect of the deposited silicon layer were systematically studied by atomic force microscopy (AFM), X-ray diffraction (XRD) and Raman spectroscopy. The thermal properties such as the thermal conductivity (K) and thermal diffusivity (D) were determined by the photo-thermal deflection (PTD) technique, which is a non-destructive technique. Based on this full characterization, it is demonstrated that the thermal and optical characteristics of this films are directly correlated to their micro-structural properties.

Keywords: Porous Aluminum; thermal conductivity; thermal diffusivity; gap energy

Article history: Received December 31, 2013; Accepted February 4, 2014

1. Introduction

In view of their practical importance, aluminum porous materials were intensively studied in the last decade with various analytical techniques (see references from 2002 by Nielsch et al., to 2012 by liu et al.). There was considerable interest primarily for the reason of its self organized pores that have quasi-cylindrical shape and well aligned and the pores sizes which are in the vicinity of nanometers range constitute a technological revolution and find now many applications such as filtration membranes such that realized by Sulka et al., 2011 or by Barbosa et al., 2012, as backing for manufacturing nanowires used by Wang et al., 2011 or Huang et al., 2012 and as photonic crystals (see for example the work of Hu et al., 2009), as humidity sensors according to Kurbanov et al., 2007 or Juhász et al., 2009 and Kashi et al.,

2012 or as cathodes for organic light emitting diodes as those of Wang et al., 2007 and Kim et al., 2008. The scientists have been focused on the fabrication of organized nano-pores by electrochemical methods by simple variation of the anodization parameters, such as voltage and electrolyte solution composition. In the literature many attempts are reported in order to find relationships between porosity, thermal properties studied by Zhuo et al., 2011 and Dyga et al., 2012, optical properties studied by Stojadinovicet al., 2009, and this by exploring the effect of size, form and density of the pores. For photovoltaic applications knowing sample emissivity, absorption and thermal properties is a primordial issue for solar energy development. It was reported also that nc-Si thin films elaborated by PECVD on a porous aluminum structure leads to the synthesis of material of great electronic quality. Thus cells based on crystalline silicon on porous aluminum offer an exciting possibility of constructing and fabricating compact photovoltaic and thermal solar collectors by direct cell deposition on a suitable porous aluminum. The fine tuning of microstructure and of the thermal properties of the elaborated films is a primordial step for controlling the functionality of the desired device. The current anodization parameter has directly an impact to the surface roughness and film density, which in turn influence the physical properties such as thermal and optical properties. The thermal properties of the deposited films are examined by photothermal deflection (PTD) technique in 1994 by Bertolotti et al., and by Ghrib et al. who have correlated them to the film microstructure. In this context, we have tailored to study the anodization current effect in the microstructure of the porous aluminium (PA) layer and the effect of the deposition of silicon layer on its optical and thermal properties.

2. Experiments processing

High-purity aluminum foil (99.997%), 0.25 mm thick was used as a starting material. Before anodizing the aluminum paper was rinsed in a CP4 solution, which is a mixture of 64% of nitric acid, 20% acetic acid CH_3COOH and 16% of fluorhydric acid to eliminate the impurities linked to the surface. The cleaned samples were treated by a mechanical polishing machine of model 920 working with different speeds combined with alumina abrasive in an alkaline solution and anodized during 25 min in a solution of diluted sulfuric acid with 66.66% H_2SO_4 and 33, 33% H_2O_2 at room temperature and with three different anodization currents (250 mA, 300 mA, 350mA). On the PA surface, c-Si was deposited by PECVD technique at 50 °C using a gas mixture of silane and H_2 at a total pressure of 0.5 m Torr. The surface morphology of the films was examined by atomic force microscopy (AFM), which has been realized in plane-view for characterizing particles on wide areas. The determination of the pore diameter and statistics has been performed with the assistance of the SWxM program. The crystal quality of porous aluminium and

the PECVD deposited c-Si was studies by means of XRD in θ-2θ configuration and confirmed by Raman spectroscopy.

The thermal properties such as the thermal conductivity and the thermal properties are determined by the PTD technique. This method whose principle is given in fig.1 consists in heating a sample with a modulated light beam of intensity $I = I_0(1 + \cos \omega t)$ that will be absorbed on the surface and generates a thermal wave. This thermal wave will propagate in the sample and in the surrounding fluid (air in our case) and will induce a temperature gradient and then a refractive index gradient in the fluid. The fluid index gradient will cause the deflection ψ of a probe laser beam skimming the sample surface. This deflection may be related to the thermal properties of the sample. The sample is heated by a halogen lamp light of Power 100 W modulated by using a mechanical chopper at a variable frequency. An (He-Ne) laser beam skimming the sample surface at a distance x is deflected. This deflection can be detected by a four quadrant photo-detector and converted to an electrical signal which is measured by a lock-in amplifier. Through the intermediary of interfaces, the mechanical chopper and the Look-in amplifier a microcomputer will set the desired modulation fre quency and read the values of the amplitude and phase of the photo-thermal signal and then draw their variations according to the square root modulation frequency.

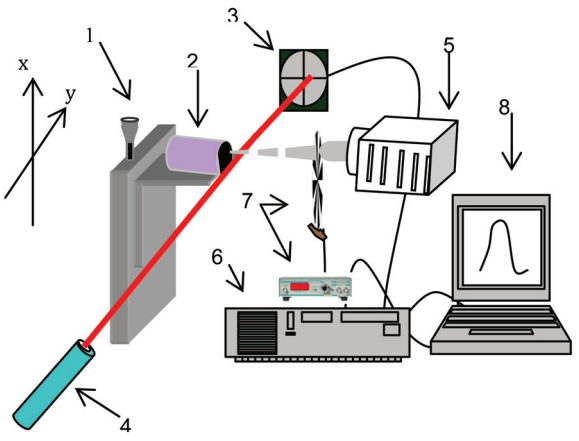

Fig. 1: Experimental set-up used for PTD investigation: 1-Table of micrometric displacement, 2-Sample, 3-Photodetector position, 4-Fixed laser source, 5-Halogen lamp, 6-Look-in amplifier, 7-Mechanical chopper, 8-Computer.

3. Results and discussions

1.1. Microstructural characterization

Fig. 2 shows AFM microscopy of these samples treated with three different anodization current intensities, in which is noted the presence of a quasi-arranged structure containing pores with width and depth varying according to the current from 24 nm for I_a = 250mA to 73 nm for I_a = 350mA.

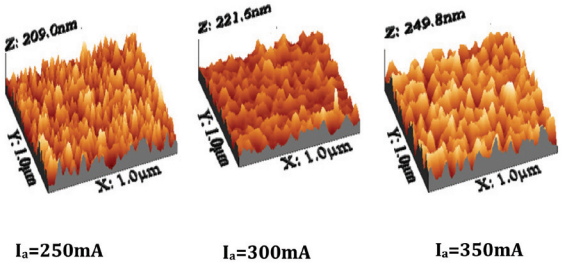

Fig. 2: AFM images of Porous Aluminum (PA) layer versus anodization current intensity(250, 300, 350) mA.

These sizes are in good accordance with those obtained by Yan-fang Xu et al., 2015, when they demonstrate that the size vary with the anodizing potential from 53nm to

130nm. Fig. 3 shows the AFM microscopy analysis indicates that the nc-Si films deposited on theses porous substrates present a nanogranular aspect with size estimated from the AFM scans from 50 to 85 nm as I_a increases.

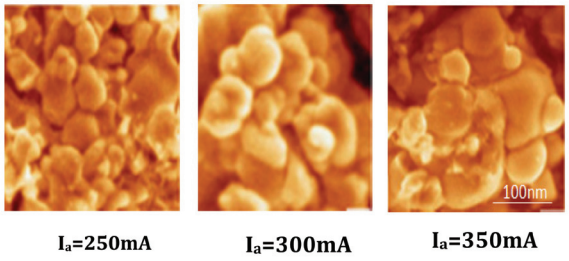

Fig. 3: AFM images of nanocrystalline silicon deposited on the porous aluminum for various anodization current intensity (250, 300, 350) mA.

Indeed, we notice two peaks indexed as the (101) and (201) direction. The two others peaks indexed as (200) and (220) are related to the aluminum substrate. The average crystallite size as deduced from the X-ray diffraction spectra using the Debey–Scherrer formula confirms the result mentioned above and increases as a function of I_a from 65 nm to 90 nm. These values are in accordance with the crystal size estimated from the AFM scans.

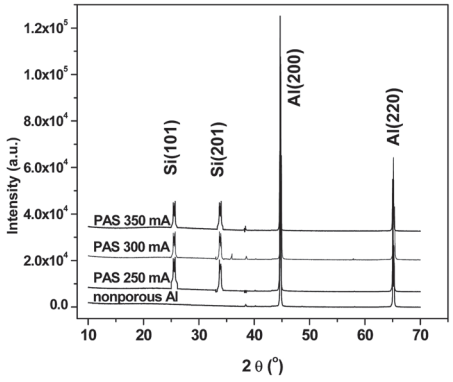

Fig. 4 shows XRD spectra for the as deposited nc-Si thin layer. The deposited silicon seems to be crystallized and presented a preferred orientation in the (h01) direction.

In order to confirm the above mentioned results in term of crystallinity and sizes of grains, the Raman spectroscopy was performed which is reported in Fig. 5 for silicon films deposited directly on nonporous aluminum and porous one in which it shows an amorphous aspect, in fact the deposited films exhibit transverse optical band of crystalline Si located near 526 cm^{-1} except for sample A1 which presents a peak at 499 cm^{-1}.

The intensity of this peak increases and its position shift to high energies with the anodizing currents tending towards a peak corresponding to monocrystalline Si at 528 cm^{-1}.

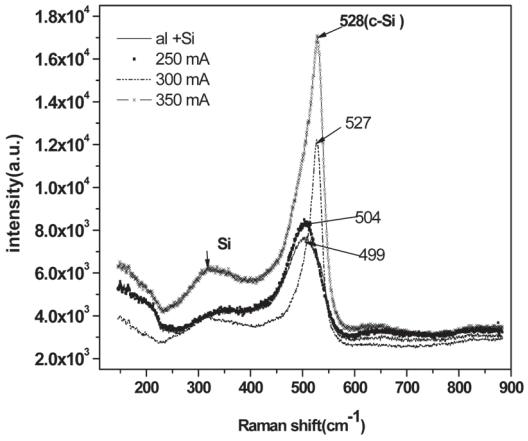

Fig. 5: Raman spectra of PASL prepared with different anodic current.

The crystallite size was calculated using the following formula.

$$\Delta w(D) = -A\left(\frac{a}{D}\right)^{\gamma} \quad (1)$$

Where $\Delta w(D) = w_{C-Si} - w_{n-Si}$ and D are the Raman peak shift in nanocrystal as compared to monocrystalline silicon; a is the lattice constant of the silicon which is equal to 0.543 nm, $A = 47.41$ and γ=1.44 are constants. The crystallite size estimated from this method was found between 75–110 nm when I_a varies from 250 to 350 mA respectively.

1.2. Thermal properties

The determination of thermal properties is made by the photo-thermal deflection technique, whose principle schema is shown in fig. 6, in which in the case of a uniform heating we have used a 1-dimensional approximation, and the amplitude and phase of the probe beam deflection is given by:

$$|\psi| = \frac{\sqrt{2}}{n}\frac{L}{\mu_f}\left|\frac{dT_f}{dx}\right|_{T_0} e^{-\frac{x}{\mu_f}} \qquad (2)$$

and

$$\varphi = -\frac{x}{\mu_f} + \theta + \frac{5\pi}{4} \qquad (3)$$

Where L is the width of the pump beam in the direction of the probe laser beam, n, μ_f and T_0 are respectively the refractive index, the thermal diffusion length and the temperature of the fluid.

The quantifies $|\square|$ and θ are respectively the amplitude and phase of the temperature at the sample surface which are function of the thermal properties of the different media. The quantity x is the distance between the probe beam axe and the sample surface. Before the calculation of the probe beam deflection, it is essential to know the expression of the surface temperature T_0 which is calculated as follow.

The sample is a stack of three layers; we write the heat equations in these three medias and in the surrounding fluid which is the air by designating K_i, D_i, and l_i, respectively, the thermal conductivity, the thermal Diffusivity and the thickness of the layer i (1: aluminum, 2: porous aluminum filled or empty, 3: silicon or air)

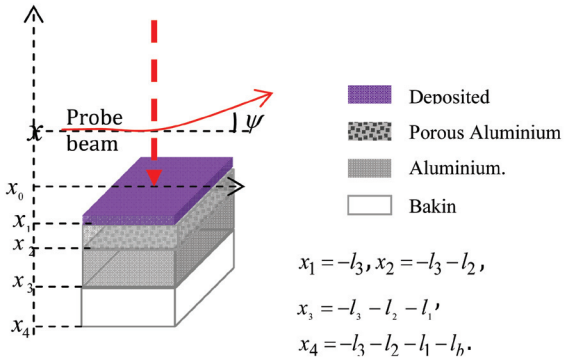

Fig. 6: The stacked three layers.

The resolution of the heat equation gives the following temperatures equations:

$$T_f(x,t) = T_0 e^{-\sigma_f x} e^{j\omega t} \quad if \;\; 0 \le x \le l_f \qquad (4)$$

$$T_3(x,t) = (X_3 e^{\sigma_3 x} + Y_3 e^{-\sigma_3 x} - E_3 e^{\alpha_3 x}) e^{j\omega t} \quad if \;\; -l_3 \le x \le 0 \qquad (5)$$

$$T_2(x,t) = (X_2 e^{\sigma_2 (x+l_3)} + Y_2 e^{-\sigma_2 (x+l_3)} - E_2 e^{\alpha_2 (x+l_3)}) e^{j\omega t} \quad if \;\; -l_3 - l_2 \le x \le -l_2 \qquad (6)$$

$$T_1(x,t) = (X_1 e^{\sigma_1 (x+l_3+l_2)} + Y_1 e^{-\sigma_1 (x+l_3+l_2)} - E_1 e^{\alpha_1 (x+l_3+l_2)}) e^{j\omega t} \quad if \;\; -l_3 - l_2 - l_1 \le x \le -l_3 - l_2 \qquad (7)$$

$$T_b(x,t) = W e^{\sigma_b (x+l_3+l_2+l_1)} e^{j\omega t} \quad if \;\; -l_3 - l_2 - l_1 - l_b \le x \le -l_3 - l_2 - l_1 \qquad (8)$$

And after, we write the flow equation in each medium:

$$\phi_f(x,t) = K_f \sigma_f T_0 e^{-\sigma_f x} e^{j\omega t} \quad if \;\; 0 \le x \le l_f \qquad (4p)$$

$$\phi_3(x,t) = -K_3 \sigma_3 (X_3 e^{\sigma_3 x} - Y_3 e^{-\sigma_3 x} - \frac{\alpha_3}{\sigma_3} E_3 e^{\alpha_3 x}) e^{j\omega t} \quad if \;\; -l_3 \le x \le 0 \qquad (5p)$$

$$\phi_2(x,t) = -K_2 \sigma_2 (X_2 e^{\sigma_2 (x+l_3)} - Y_2 e^{-\sigma_3 (x+l_3)} \frac{\alpha_2}{\sigma_2} E_2 e^{\alpha_2 (x+l_3)}) e^{j\omega t} \quad if \;\; -l_3 - l_2 \le x \le -l_2 \qquad (6p)$$

$$\phi_1(x,t) = -K_1 \sigma_1 (X_1 e^{\sigma_1 (x+l_3+l_2)} - Y_1 e^{-\sigma_2 (x+l_3+l_2)} \frac{\alpha_1}{\sigma_1} E_1 e^{\alpha_1 (x+l_3+l_2)}) e^{j\omega t} \quad if \;\; -l_3 - l_2 - l_1 \le x \le -l_3 - l_2 \qquad (7p)$$

$$\phi_b(x,t) = -K_b \sigma_b W e^{\sigma_b (x+l_3+l_2+l_1)} e^{j\omega t} \quad if \;\; -l_3 - l_2 - l_1 - l_b \le x \le -l_3 - l_2 - l_1 \qquad (8p)$$

The temperature and heat flow continuity at the interfaces $x = -l_3, -l_3 - l_2$, permit to obtain:

$$\begin{bmatrix} 1 & 1 & -1 \\ 1 & -1 & -r_2 \\ 0 & 0 & E_3/E_2 \end{bmatrix} \begin{bmatrix} X_2 \\ Y_2 \\ E_2 \end{bmatrix} = \begin{bmatrix} e^{-\sigma_3 l_3} & e^{\sigma_3 l_3} & -e^{-\alpha_3 l_3} \\ c_3 e^{-\sigma_3 l_3} & -c_3 e^{\sigma_3 l_3} & -c_3 r_3 e^{-\alpha_3 l_3} \\ 0 & 0 & 1 \end{bmatrix} \begin{bmatrix} X_3 \\ Y_3 \\ E_3 \end{bmatrix}$$

$$G_3 \begin{bmatrix} X_2 \\ Y_2 \\ E_2 \end{bmatrix} = D_3 \begin{bmatrix} X_3 \\ Y_3 \\ E_3 \end{bmatrix} \quad \text{i.e.}$$

$$\begin{bmatrix} X_2 \\ Y_2 \\ E_2 \end{bmatrix} = G_3^{-1}.D_3 \begin{bmatrix} X_3 \\ Y_3 \\ E_3 \end{bmatrix} = M_3 \begin{bmatrix} X_3 \\ Y_3 \\ E_3 \end{bmatrix}$$

Where

$$G_3 = \begin{bmatrix} 1 & 1 & -1 \\ 1 & -1 & -r_2 \\ 0 & 0 & E_3/E_2 \end{bmatrix},$$

$$D_3 = \begin{bmatrix} e^{-\sigma_3 l_3} & e^{\sigma_3 l_3} & -e^{-\alpha_3 l_3} \\ c_3 e^{-\sigma_3 l_3} & -c_3 e^{\sigma_3 l_3} & -c_3 r_3 e^{-\alpha_3 l_3} \\ 0 & 0 & 1 \end{bmatrix}$$

and $M_3 = G_3^{-1}.D_3$

In the same way we can write

$$\begin{bmatrix} X_1 \\ Y_1 \\ E_1 \end{bmatrix} = G_2^{-1}.D_2 \begin{bmatrix} X_2 \\ Y_2 \\ E_2 \end{bmatrix} = M_2 \begin{bmatrix} X_3 \\ Y_3 \\ E_3 \end{bmatrix}$$

Where

$$G_2 = \begin{bmatrix} 1 & 1 & -1 \\ 1 & -1 & -r_1 \\ 0 & 0 & E_2/E_1 \end{bmatrix} \text{ and}$$

$$D_2 = \begin{bmatrix} e^{-\sigma_2 l_2} & e^{\sigma_2 l_2} & -e^{-\alpha_2 l_2} \\ c_2 e^{-\sigma_2 l_2} & -c_2 e^{\sigma_2 l_2} & -c_2 r_2 e^{-\alpha_2 l_2} \\ 0 & 0 & 1 \end{bmatrix}$$

Then

$$\begin{bmatrix} X_1 \\ Y_1 \\ E_1 \end{bmatrix} = M_2.M_3 \begin{bmatrix} X_3 \\ Y_3 \\ E_3 \end{bmatrix} = \begin{bmatrix} m_{11} & m_{12} & m_{13} \\ m_{21} & m_{22} & m_{23} \\ m_{31} & m_{32} & m_{33} \end{bmatrix} \begin{bmatrix} X_3 \\ Y_3 \\ E_3 \end{bmatrix}$$

In this case we write

$$\begin{cases} X_1 = m_{11}X_3 + m_{12}Y_3 + m_{13}E_3 \\ Y_1 = m_{21}X_3 + m_{22}Y_3 + m_{23}E_3 \end{cases}$$

The writing of the heat flow and temperature continuity at the interfaces x_0 and x_3 give respectively:

$$X_3 = \frac{1}{2}(1-g)T_0 + (1+r_3)\frac{E_3}{2},$$

$$Y_3 = \frac{1}{2}(1+g)T_0 + (1-r_3)\frac{E_3}{2} \text{ and}$$

$$(1-b)\,e^{-\sigma_1 l_1}X_1 - (1+b)\,e^{\sigma_1 l_1}Y_1 - (r_1-b)e^{-\alpha_1 l_1}E_1 = 0 \qquad (9).$$

Then

$$X_1 = \frac{m_{11}}{2}((1-g)T_0 + (1+r_3)E_3) + \frac{m_{12}}{2}((1+g)T_0 + (1-r_3)E_3) + m_{13}E_3$$

and

$$Y_1 = \frac{m_{21}}{2}((1-g)T_0 + (1+r_3)E_3) + \frac{m_{22}}{2}((1+g)T_0 + (1-r_3)E_3) + m_{23}E_3$$

.

Or otherwise

$$X_1 = (m_{11}(1-g) + m_{12}(1+g))\frac{T_0}{2} + (m_{11}(1+r_3) + m_{12}(1-r_3) + 2m_{13})\frac{E_3}{2}$$

and

$$Y_1 = (m_{21}(1-g) + m_{22}(1+g))\frac{T_0}{2} + (m_{21}(1+r_3) + m_{22}(1-r_3) + 2m_{23})\frac{E_3}{2}$$

.

That give $X_1 = \eta_1 T_0 + \eta_2 E_3$ and $Y_1 = \eta_3 T_0 + \eta_4 E_3$

By replacing X_1 and Y_1 by its expressions in Eq. 9, one obtains:

$$(1-b)\,e^{-\sigma_1 l_1}(\eta_1 T_0 + \eta_2 E_3) - (1+b)\,e^{\sigma_1 l_1}(\eta_3 T_0 + \eta_4 E_3) - (r_1-b)e^{-\alpha_1 l_1}E_1 = 0$$

This gives

$$((1-b)\eta_1 e^{-\sigma_1 l_1} - (1+b)\eta_3 e^{\sigma_1 l_1})T_0 = ((1+b)\eta_4 e^{\sigma_1 l_1} - (1-b)\eta_2 e^{-\sigma_1 l_1})E_3 + (r_1-b)e^{-\alpha_1 l_1}E_1$$

Finally

$$T_0 = [((1+b)\eta_4 e^{\sigma_1 l_1} - (1-b)\eta_2 e^{-\sigma_1 l_1})E_3 + (r_1-b)e^{-\alpha_1 l_1}E_1] / [((1-b)\eta_1 e^{-\sigma_1 l_1} - (1+b)\eta_3 e^{\sigma_1 l_1})] \qquad (10)$$

In order to determine the thermal properties evolutions with the anodization current before and after the silicon deposition we have studied the variation of the photo-thermal signal with the square root modulation frequency for different samples.

To determine the changes of thermal properties of aluminum we start by determining the thermal properties such as the thermal conductivity K_2 and thermal diffusivity D_2 of the PA and we study the variation of the photo thermal signal for the same samples, which were filled by the silicon (PAS). The experimental variations of the amplitude and phase of photothermal signal are given respectively in Fig. 7 and 8.

To determine the thermal properties we have used the model with three layers (aluminum/(porous aluminum filled with silicon)/silicon) and we begin in a first step by introducing thermal properties of the deposited layer which are $(K_3 = 0.15\, W.K^{-1}.m^{-1}, D_3 = 0.38 \times 10^{-4}\, m^2.s^{-1})$ for the silicon nanocrystalline and $(K_3 = 0.022\, W.K^{-1}.m^{-1}, D_3 = 0.2 \times 10^{-4}\, m^2.s^{-1})$ for the empty porous aluminum and we introduce the thermal properties of the nonporous aluminum which are $(K_1 = 273\, W.K^{-1}.m^{-1}, D_1 = 0.94 \times 10^{-4}\, m^2.s^{-1})$ and in second step we compare the experimental signal with its corresponding theoretical, whereby the best fitting gives the values of the pair (K_2, D_2).

After the simulation of the curves of figs. 7 and 8 the obtained values are given in Table 1 for the porous aluminum empty and filled with silicon, in which it is noted that they decrease with the anodization current for tending toward an average value of about 131 $W.m^{-1}.K^{-1}$ for both the porous aluminum empty or filled with silicon which characterizes the semiconductor material; for this, we can say that the introduction of thermal isolator material such as air or nc-Si in aluminum which is considered as a thermal conductor transforms it toward a thermal semiconductor.

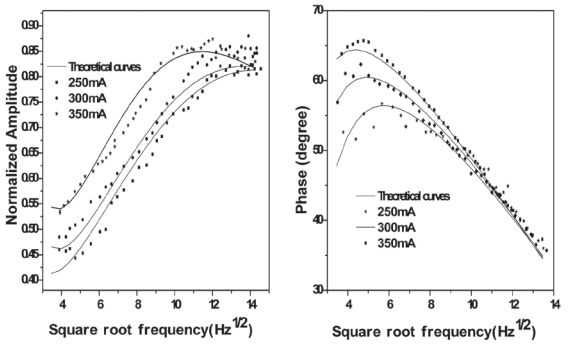

Fig. 7: Experimental and theoretical variation of the photothermal signal for the empty porous aluminum.

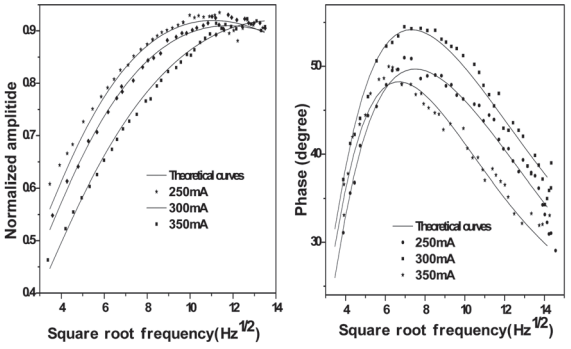

Fig. 8: Experimental and theoretical variation of the photothermal signal for the porous aluminum treated with deferent anodization current and filled with crystalline silicon.

Knowing the conductivity of porous layer can calculate the percentage of pores in the treated sample by using the Eq. 10, whose values are given in Table 1 where we remark its increase with anodizing current and has the same magnitude by using thePA or PAS values.

$$= \frac{K_2 - K_1}{K_3 - K_1} \quad (10)$$

Table 1: Measured thermal properties, calculated porous density of the empty porous aluminum and porous aluminum filled with silicon and its gap energy for different anodization current intensities (250,300,350) mA.

	Empty Porous Aluminum			Porous aluminum filled with silicon		
I_a	250mA	300mA	350mA	250mA	300mA	350mA
$K_z(W\,m^{-1}K^{-1})$	155.6±6	143±4	133 ± 5	160 ± 6	142 ± 5	132 ± 3
$D_z(cm^2s^{-1})$	0.59±0.04	0.46 ± 0.04	0.39±0.04	0.63±0.03	0.42± 0.03	0.38±0.03
$\varepsilon(\%)$	43.1%	48.0%	52.1%	41.4%	48.0%	52.0%
$E_g(eV)$	-	-	-	2.03	2.01	1.99

1.3. Energy gap

Both the two materials PA and PAS are thermal semiconductors but only the PAS is an electrical semiconductor in which its energy gap is determined by using the Tauc method which implies that for energies **E=hv** higher than the energy gap E_g, the quantity $(\alpha E)^n$ varies with E according the relationship $(\alpha E)^n=\beta(E-E_g)$ where α is the absorption coefficient and b is the slope of the curve. For indirect band gap semiconductor such as nanocrystalline Si (nc-Si) deposited on porous aluminum $n=\frac{1}{2}$. Then the curves of $(\alpha E)^{1/2}$ versus E are shown in Fig. 9 on which it is indicated the linear part, whose intersection with the abscissa axis gives the energy gap.

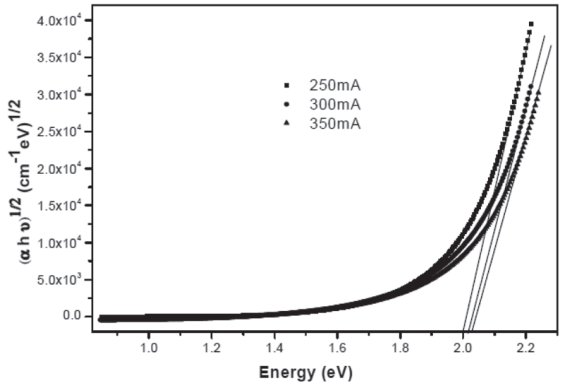

Fig. 9: Typical plot of $(\alpha E)^{1/2}$ function versus photon energy with linear curves giving the PAS energy gap for various current intensities.

The obtained values are reported in Table 1 which shows that the energy gap decreases with the anodizing current from 2.03 to 1.99 eV marking a shift of about 40 meV; which has a more importance than that obtained for other works where we obtain a semiconductor with stable structure and middle gap energy whose its decrease can be attributed to the increase in porosity rate which is due to a decrease in the mean free path due to the phonon confinement in crystallite demonstrated and used by Lin et al., 2014 and Yao et al., 2015.

4. Conclusion

Nano-crystallines silicon (nc-Si) whose sizes in 30–70 nm range were deposited by PECVD technique on porous aluminum (PA) layers which were prepared by the anodization technique for various current intensities. XRD, AFM and Raman measurements show that the pores are of cylindrical shape in the direction of the anodization current and presenting a diameter around 40 nm which increase with the anodization current intensity. Filling these pores with nc-Si transforms the aluminum material in its surface from a conductor to a semiconductor material whose energy gap is about 2eV has experienced a decrease of about 40 meV with increasing the porous density; and the thermal conductivity and diffusivity were determined by the photothermal deflection technique whose principle is described in detail which shows that they decrease with the porous density. This material has made the structural and

physical properties that allow it to be used in several energetic fields such as solar cells and heat exchangers.

Acknowledgements

This work was supported by the Scientific Research Deanship of University of Dammam, under Project no. 2014264.

References

NielschK., ChoiJ., SchwirnK., WehrspohnR. B., and GoseleU., Nano. Lett. 2)2002(677-680.

VrublevskyI., ParkounV., SchreckenbachJ., MarxG., Applied Surface Science 220 (2003) 51-59.

GalcaA. C., KooijE. S., WormeesterH., and SalmC., Journal of applied physics 94 (2003) 4296-4305.

TsengW. J.TsaiC. J., Journal of Materials Processing Technology, 146 (2004) 289-293.

RamJ., SinghR., Applied Thermal Engineering 24 (2004) 2727–2735.

KuA. Y., TaylorS. T., HewardW. J., DenaultL., LoureiroS. M., Microporous and Mesoporous Materials 88 (2006) 214-219.

SamantrayP. K., KarthikeyanP., ReddyK.S., International Journal of Heat and Mass Transfer 49 (2006), 4209–4219.

WangT. C., FanT. X., ZhangD., ZhangG. D., XiongD. S., Materials Letters 61 (2007) 1849–1854.

AlinejadB., ZakeriM., Journal of Materials Processing Technology 209 (2009) 5042-5045.

MurpheyM.B., BergesonJ.D., EtzkornS.J., QuL., LiL., DaiL., EpsteinA.J., Synthetic Metals 160 (2010) 235-237.

GhribM., GaidiM., KhedherN., GhribT., Ben SalemM., EzzaouiaH., Applied Surface Science 257 (2011) 3998-4003.

LiuW., CanfieldN., Journal of Membrane Science 409–410 (2012) 113-126.

SulkaG. D., BrzózkaA., LiuL., ElectrochimicaActa 56 (2011) 4972-4979.

BarbosaE. F., SilvaL. P., Journal of Membrane Science 407–408 (2012), 128-135.

WangX., LiC., ChenG., HeL., CaoH., ZhangB., Solid State Sciences 13 (2011) 280-284.

HuangJ., RenH., SunP., GuC., SunY., LiuJ., Sensors and Actuators B: Chemical 188 (2013) 249-256.

HuX., PuY.J., LingZ.Y., LiY., Optical Materials 32 (2009) 382-386.

KurbanovS.S., Shaymardanov Z. S., KasymdzhanovM.A., KhabibullaevP.K., KangT.W., Optical Materials 29 (2007) 1177-1182.

JuhászL., MizseiJ., Thin Solid Films 517 (2009) 6198-6201.

Kashi M. A., RamazaniA., AbbasianH., KhayyatianA., Sensors and Actuators A: Physical 174 (2012) 69-74.

WangT. C., FanT. X., ZhangD., Zhang G., XiongD. S., Materials Letters 61 (2007)1849-1854.

KimK.P., LeeK.S., KimT.W., Woo D.H., Kim J.H., SeoJ.H., KimY.K., Thin Solid Films 516 (2008) 3633–3636.

ZhuoH., PengF., LinL., QuY., LaiF., Thin Solid Films 519 (2011) 2308-2312.

DygaR., WitczakS., Procedia Engineering 42 (2012)1088-1099.

StojadinovicS., NedicZ., BelcaI., VasilicR., KasalicaB., PetkovicM., Zekovic L. j., Applied Surface Science 256 (2009) 763-767.

BertolottiM., LiakhouG. L., FerrariA., RalchenkoV. G., SmolinA. A., obrastsovaE., KorotoushenkoK. G., PimenovS. M., KonovV. I., J. Appl. Phys. 75 (1994) 7795-7798.

GhribT., BejaouiF., HamdiA., YacoubiN., ThermochimicaActa 473 (2008) 86–91.

GhribT., GaiedI., YacoubiN., Nondestructive Testing: Methods, Analyses and Applications, eBooks, Nova publishers (2010) 95-146.

Xu Y. F., Liu H., Li X. j., KangW. M., ChengB. W., LiX. J., Materials Letters 151 (2015) 79–81.

LinY. C., ChaoY. T., YaoP.-C., Appl. Surf. Sci. 307 (2014) 724-730.

YaoP. C., ChenC. Y., Thin Solid Films 579 (2015) 103–109.

Quantitative and Qualitative Analysis of Sand in Nafud Desert at Zilfi Province using (ICP-MS) Spectroscopic Technique

Nawal M. Suleman*
Chemistry Departement, College of Education, Majmaah University, Zilfi, 11932, P.O 1221, Saudi Arabia, n.suleman@mu.edu.sa

I. ElAgib
Physics Departement, College of Science, King Saud University, Riyadh, 11451, P.O 2455, Saudi Arabia, elagib@ksu.edu.sa

Abstract

In this present study soil samples were collected from an agriculture area of Zilfi Province of Saudi Arabia approximately 260 km northwest, of the capital city Riyadh. The area of study (Nafud Desert in Zilfi Province) was surveyed during December 2012 collecting 21 samples from 7 places (Al sabla, Almata, Jaway, Alaaga, Magra, Shlwan, and Althuare, by taking 3 samples from each place at the surface, 20 cm and 40 cm depth .The concentrations of some elements such as Si, Na, Mg, Ca, K, Al, P, S, Ti, V, Mn, Fe, Ni, Cu, As, Au, Pb, Cr, Co, Cd and Zn were measured , using Inductively Coupled Plasma-Mass Spectrometer (ICP-MS), after sieving and digestion using HNO3, HCL and HF. In most of the samples the elements (Au or Cd), found to have low concentrations while the element S found to be has the high concentrations. The concentrations of toxic trace elements (Ni, Cd and As), were found have values more than back ground concentrations found in the literature of sandstone. The maximum concentrations of the elements: Pb, Zn, Na, Ca and Cd were found at Al sabla region. On the other hand, the maximum concentrations of the elements: As, and V were found in Shlwan region, while the maximum concentration of Cr was found in Alaaga region. Magra region shows maximum concentrations of elements Au, Si, Ti, P, Al, Fe, Mg,and S. High concentration of elements Cu, Mn and K were found in Althuare region, while Ni in Jaway region, and Co in Magra and Althuare regions.

Keywords: Porous media, mass transfer, magnetic field, non-Newtonian fluid

Article history: Received: March6, 2013, Accepted: December, 2015

1. Introduction

Zilfi Province is located to the North of Riyadh, capital of Saudi Arabia approximately 260 km northwest, being in the middle of the Arabian Desert.Quartzose sands with very poor heavy-mineral suites including zircon occupy most of the region comprising the Great Nafud and Rub al-Khali Sand Seas and are largely recycled from thick lower Paleozoic quartzarenites with very minor first-cycle contributions from Precambrian basement, Mesozoic carbonate rocks, or Neogene basalts [1].

Silicon comprises about 28% of the lithosphere and is next to oxygen, the most abundant element. It is found as the oxide

in crystalline forms, as in quartz; combined with other oxides and metals in a variety of silicates; and in amorphous forms. Silicon is the most abundant element in igneous rocks and is the characteristic element of all important rocks except the carbonates.

Silica is used primarily in the production of glass for windows, drinking glasses, beverage bottles, and many other uses. The majority of optical fibers for telecommunications are also made from silica. It is a primary raw material for many white ware ceramics Silica is a common additive in the production of foods, where it is used primarily as a flow agent in powdered foods, or to absorb water in hygroscopic applications. It is the primary component of diatomaceous earth which has many uses ranging from filtration to insect control. It is also the primary component of rice husk ash which is used, for example, in filtration and cement manufacturing. Therefore, the study of chemical components and physical properties of the sand found at Nafud dessert in Zilfi province using, (ICP-MS), is carried out.

Silica is most commonly found in nature as sand or quartz. Silica sand is a white or colorless crystalline compound, occurring abundantly as quartz, sand, flint, agate and in many minerals .It is used as an essential raw material in the production of glass, foundry, abrasives, filters, and ceramics, in chemical and hydraulic fracturing and on oil fields [2]. Silica sand contains Al, Fe, Ti, Ca, Mg, Mn, Na and K as impurities in varying quantities. Iron, aluminum and titanium impurities can alter the color, chemical, optical and mechanical properties of the product [3,4].In common glass and allied materials; Al is associated with moderate to low quantities of Ti and Fe. For such materials, the quantities of these metals are determined separately by complexometric and colorimetric methods [5]. In the direct titrations however, Al, Ti and Fe interact with one another. Several instrumental techniques such as inductively coupled plasma (ICP) emission and atomic absorption spectrometry (AAS) in such matrixes have been adopted for the determination of the trace metallic impurities [6-9].Voinovitch, have determined Al in the presence of Ti and Fe by employing an excess of EDTA with $ZnCl_2$ as the back titrant at pH 5–6 (in presence of tartaric acid, diammonium phosphate and fluoride) and dithiozoneindicator [10]. In using this method it has been observed that the end point can be affected by the reaction of tartaric acid with Zn as well as dithiozone indicator's slight ability to absorb titanium phosphate. Miles summarized the quantitative analysis of quartz by IR methods[11]. All analytical methods for crystalline silica analysis (XRD, IR and UV-VIS) are particle size dependent, as summarized [12].The concentration of lead, zinc, cadmium, nickel, copper and vanadium in the sediments of nineteen coastal stations in Bahrain were determined by atomic absorption spectrophotometer (AAS) [13]. Several samples of environmental concern were analyzed for trace element content by instrumental neutron activation analysis (INAA) in Tunisian soil, desert and beach sand

[14]. Multivariate cluster analysis of some major and trace elements distribution in an unsaturated zone profile, Densu River Basin, Ghana was done using Energy Dispersive X-ray Fluorescence (EDXRF)[15].Grain-size distribution and chemical analyses were carried out on four sand samples randomly taken from the bank of Otamiri River around Chokocho and Umuanyaga, Etche Local Government Area, Rivers State. This was done to assess the purity and suitability of the sands for the making of plain glass [16]. Soil samples containing `Amang` were taken to recover its heavy minerals by separating them into individual minerals, sample containing monazite, ilmenite, and zircon were separated by 8000 G hand magnet. The morphology of each mineral was investigated by computer controlled scanning electron microscopy coupled with an energy-dispersive X-ray detector (CC-SEM/EDX) [17].

Inductively Coupled Plasma-Mass Spectrometry (ICP-MS) technique was used to determine the concentrations of titanium (Ti), vanadium (V), Chromium (Cr), Manganese (Mn), iron (Fe), zinc (Zn), arsenic (As), zirconium (Zr), cadmium (Cd) and hafnium (Hf) in black sands samples [18].

2. Materials and Methods

2.1. Instrumentation

The analytical determination of Si, Na, Mg, Ca, K, Al, P, S, Ti, V, Mn, Fe, Ni, Cu, As, Au, Pb, Cr, Co, Cd and Zn was carried out by ICP-MS(Inductively Coupled Plasma-Mass Spectrometer): ELAN 9000 (Perkin Elmer Sciex Instrumento, Concord, Ontario, Canada). Table1 highlights the operating conditions of the instruments used in this study.

Table 1. Conditions of ELAN 9000 ICP-MS

RF power	1250 W
Nebulizer gas flow	0.92 L/min
Lens Voltage	9.25 V
Analog Stage Voltage	-1762.5 V
Pulse Stage Voltage	1050 V
Number of Replicates	3
Reading / Replicates	20
Scan Mode	Peak Hopping
Dwell Time	40 ms
Integration	1200ms

2.2. Reagents

Nitric acid (69 % v/v), super purity grade from Romil, England. Hydrochloric acid (37% v/v) and hydrofluoric acid (40% v/v) were procured from Merck Germany. High purity water obtained from Millipore Milli-Q water purification system was used throughout the work.

2.3. Calibration

The ICP-MS calibration was carried out by external calibration with the blank solution and three working standard solutions (20,40 and 60 ppm),starting from a 1000mg/l single standard solutions for ICP-MS (A raster grade, BDH laboratory supplies, England for the elements: Si, Na, Mg, Ca, K, Al, P, S, Ti, V, Mn, Fe, Ni, Cu, As, Au, Pb, Cr, Co, Cd and Zn.)

2.4. Sample collection and preparation

The area of study (Nafud Desert in Zilfi Province) was surveyed during December 2012 collecting 21 samples from 7 places (Alsabla, Almatal, Jaway, Alaaga, Magra, Shlwan and Althuare) by taking 3 samples from each place at the surface, 20 cm and 40 cm depth. The samples were transferred to plastics bags, and sieved through 200 mm thieve. Samples were prepared by accurately weighing around 200 mg of sand samples into a dry and clean Teflon digestion beaker, 6 ml of HNO_3,2 ml HCl and 2 ml HF were added to the Teflon beaker. Samples were digested on the hot plate at 120-150˚C for approximately 40 minutes. The resulting digest was not clear, so it was filtered through Whitman filtered paper no.42.The filtered digest was transferred to a 50 ml plastic volumetric flask and made up to mark using deionized water. A blank digest was carried out in the same way.

2.5. pH Determination method

An amount of 20 g of dry sieved sample were stirred with ultra-pure distilled water (50 ml) and left to equilibrate over a period of 30 minutes, and then the pH of each sample was measured using a microprocessor pH meter (HANN PH 210). Table 2 lists selected districts for sand sampling points. The soils were classified as moderately alkaline. The soil depth of 20-40 cm registered the highest pH, especially in Al sabla, Shlwan, Jaway and Magra regions. Almatal, Alaaga, and Althuare regions have a higher pH at surface.

Table2. The selected areas for sand sampling points

Dust sample	Sampling site	pH
1	Alsabla at surface	8.72
2	Alsabla (20 cm underground)	8.89
3	Alsabla (40 cm underground)	9.08
4	Almatal at surface	9.21
5	Almatal (20 cm underground)	8.91
6	Almatal (40 cm underground)	9.04
7	Shlwan at surface	9.10
8	Shlwan (20 cm underground)	9.25
9	Shlwan (40 cm underground)	9.31
10	Alaaga at surface	9.05
11	Alaaga (20 cm underground)	9.02
12	Alaaga (40 cm underground)	8.97
13	Jaway at surface	9.12
14	Jaway (20 cm underground)	9.23
15	Jaway (40 cm underground)	9.09
16	Magra at surface	9.11
17	Magra (20 cm underground)	9.18
18	Magra (40 cm underground)	9.18
19	Althuare at surface	8.94
20	Althuare (20 cm underground)	8.92
21	Althuare(40 cm underground)	8.87

3. Results and Discussion

Elemental analyses for 21 sand samples were performed by using inductively coupled Plasma-mass spectrometer (ICP-MS). All calibration graphs are linear in the selected range of each element. The square of the correlation (R^2) ranges from 0.9985-0.099999 for most of the elements in this investigation. Good precision values were obtained. The results have been reviewed in Tables (3-10) and Figures (1-4).

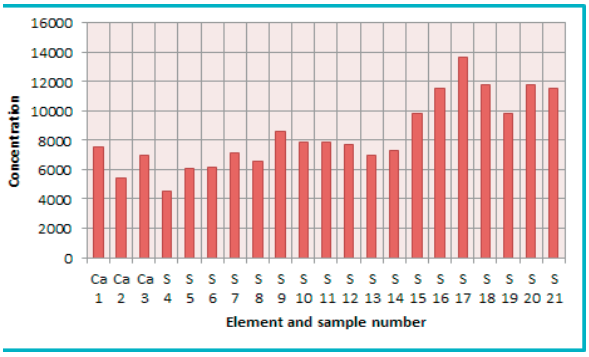

Fig.1: Comparison between maximum concentrations found in sand samples

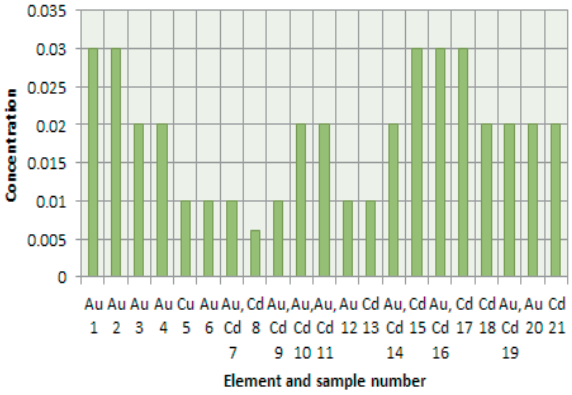

Fig. 2: Comparison between minimum concentrations found in sand samples

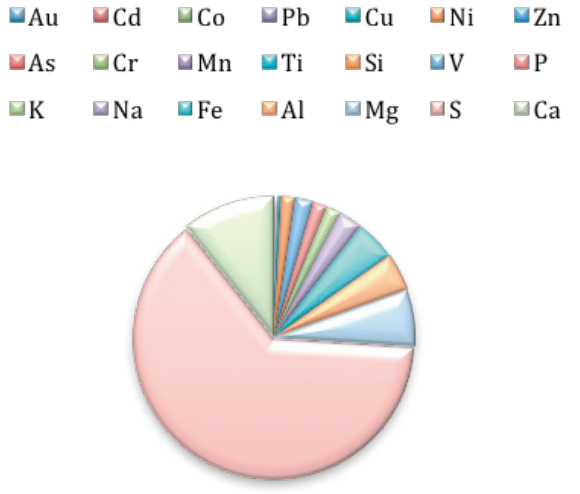

Fig. 3: Element minimum concentrations in sand samples

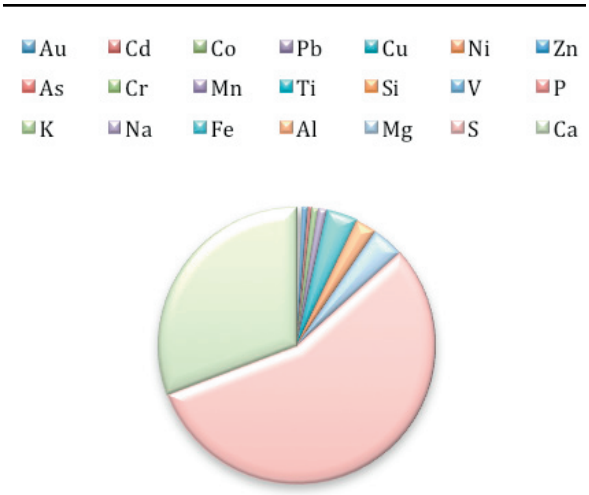

Fig. 4: Element maximum concentrations in sand samples

Magra region at surface contains the higher number of maximum concentrations elements: Co, Ti, P, Fe, Al and Mg. While Shlwan area sample (9), 40 cm depth, contains the maximum number of low elements concentrations which are: Au, Co, Pb, Ni and Fe, also this sample have the higher pH (9.30) over all samples which may be as a result of these elements. In all samples the elements (Au or Cd) represents the low concentrations except sample (5) which have the element (Cu) with low concentration. In samples (1-3) the maximum concentration element is Ca, while the element S shows high concentrations in the rest of the samples.

The concentrations of the elements: Au, Cd, Cu, Ni and V are found to be closed to the concentrations of these elements in the study which include a method of quantitative analysis for the determination of some metals in soils from Northern California by ICP-MS [19]. Also the concentrations of the elements: Zn, Mn, and P in this study are in agreement

with the study that used ICP-MS as a method of quantitative analysis for the determination of some metals (As, Ni, Cd, Ag, Pb, Zn, Mn, Sr, Co, Ga, V, Rb, U, Li, Cu) in soils [20]. This study agrees with the study of the Egyptian Black Sands from Abu Khashaba [18] Beach Area that considered ICP-MS as a good technique for its high efficiency of the detection of the trace elements.

The concentrations of toxic trace elements specially (Ni, Cd and As), have concentrations more than back ground values found in the literature of sandstone [21]. According to the study by Suleman et. al. [22, 23] which measured out some trace elements in street dust at Zilfi, the concentration of As was found to be more than the allowed value in literature; this may due to geological nature in this area. The rest of the trace elements (Co, Pb, Cu, Zn, and Cr) have been found less than allowed concentrations in literature, this may due to the fact that these areas under study are far away from pollution. The maximum concentrations of the elements: Pb, Zn, Na, Ca, and Cd are found at Al-Sabla region; this can be attributed to, location of this region next to the city and thus more exposed to contamination from cars and industrial area. On the other hand, the maximum concentrations of the elements: As, and V, are found in Shlwan region, while the maximum concentration of Cr was found in Alaaga region. Magra region contains Au, Si, Ti, P, Al, Fe, Mg, and S maximum concentrations. Cu, Mn, and K maximum concentrations are lie in Althuare, Ni at Jaway, and Co at Magra and Althuare. The minimum concentrations of the elements are as follows: Au (Almatal, Shlwan and Alaaga regions) Cd and Fe (Shlwan region), Co and Pb (Almatal and Shlwan region), Cu, Zn, P, Mn and Ca (Almatal region), Ni (Shlwan, Alaaga ,and Jaway regions), As, V and S (Alsabla region), Cr (Althuare region), Ti and Na (Alaaga region), Si and Al (Magra region), K and Mg (Jaway region).

Table3.Elements concentration in sand samples (µg/g) = (mg/Kg) = (ppm)

Sample No.	1	2	3
Element	Mean Concentration±SD		
Au	0.03±0.001	0.03±0.001	0.02±0.001
Cd	0.05±0.002	0.06±0.003	0.04±0.002
Co	0.1±0.003	0.09±0.003	0.1±0.004
Pb	0.14±0.006	0.09±0.004	0.1±0.004
Cu	0.6±0.02	0.2±0.007	0.4±0.02
Ni	1.4±0.05	1.2±0.04	1.4±0.04
Zn	4.2±0.1	1.5±0.05	3.4±0.12
As	4.6±0.2	4.8±0.2	5.0±0.11
Cr	4.8±0.2	5.7±0.2	6.5±0.2
Mn	11.5±0.4	8.0±0.3	10.4±0.3
Ti	19.5±0.8	18.6±0.4	18.9±0.5
Si	43.3±0.4	43.8±0.5	43.5±0.9
V	55.1±1.5	55.2±2	63.6±1.1
P	61.4±2	76.9±1.4	88.6±1.6
K	94.0±2	83.4±2.6	90.0±1.0
Na	157.7±4	159.4±2.6	258.2±2.1
Fe	424.7±8	383.5±7.3	408.9±4.1
Al	455.0±6	428.4±14	449.0±9.9
Mg	536.3±16	530.0±10.6	671.7±8.1
S	1721±25	2445.0±41	3239.1±29
Ca	7534.0±113	5431.9±135	6949.7±35

Table4. Elements concentration in sand samples (µg/g) =(mg/Kg) = (ppm)

Sample No.	4	5	6
Element	Mean Concentration±SD		
Au	0.02±0.001	0.01±0.001	0.01±0.0005
Cd	0.03±0.001	0.02±0.001	0.02±0.001
Co	0.05±0.002	0.03±0.001	0.04±0.001
Pb	0.05±0.002	0.05±.002	0.04±.002
Cu	0.2±0.01	0.05±0.002	0.04±0.002
Ni	0.7±0.03	0.5±0.02	0.6±0.02
Zn	0.7±0.03	0.7±0.03	0.7±0.03
As	4.5±0.2	4.1±0.1	3.6±0.1
Cr	4.8±0.16	5.0±0.16	5.6±0.1
Mn	7.2±0.3	8.1±0.3	9.2±0.3
Ti	13.3±0.2	11.4±1.2	12.1±0.4
Si	44.0±0.6	44.1±0.8	43.9±0.9
V	45.9±1.3	43.7±1.2	45.3±1.2
P	100.1±3.1	47.5±1.5	48.4±1.0
K	105.2±3.3	111.9±4.1	116.0±1.4
Na	123.5±2.3	134.1±3.2	125.0±2.6
Fe	169.4±2.0	134.3±3.2	135.2±2.0
Al	268.7±6.7	225.7±6.8	232.6±5.3
Mg	311.6±6.2	280.3±9.5	261.6±2.9
S	380.3±5.7	289.4±7.5	452.0±15
Ca	4547.5±45.5	6104.0±61	6153.1±5.2

Table 5. Elements concentration in sand samples (µg/g) = (mg/Kg) = (ppm)

Sample No.	7	8	9
Element	Mean Concentration±SD		
Au	0.01±0.0004	0.006±0.0002	0.01±0.0005
Cd	0.01±0.0004	0.02±0.001	0.01±0.004
Co	0.06±0.003	0.05±0.002	0.04±.002
Pb	0.09±.004	0.05±.004	0.04±0.002
Cu	0.1±0.004	0.1±0.004	0.2±0.0006
Ni	0.7±0.02	0.4±0.02	0.4±0.01
Zn	1.6±0.05	1.1±0.04	0.8±0.03
As	5.0±0.2	4.2±0.1	4.3±0.1
Cr	5.6±0.2	4.8±0.12	5.7±0.2

Table 5. contd.

Mn	10.9±0.5	8.8±0.2	9.9±0.3
Ti	14.9±0.3	11.7±0.3	12.3±0.2
Si	44.3±0.9	44.2±1.0	43.8±0.5
V	55.7±1.6	45.3±1.2	49.6±1.0
P	85.0±2.1	69.7±2	57.1±1.1
K	144.1±2.2	118.0±1.4	126.6±2.3
Na	215.0±2.8	158.7±2.9	152.1±3.5
Fe	216.7±5.9	170.6±2.7	159.3±2.2
Al	320.5±4.5	282.0±10.7	243.2±6.5
Mg	386.3±8.1	348.0±7.7	297.8±3.3
S	1301.1±11.7	644.8±9.0	645.2±9.7
Ca	7116.0±7.1	6532.6±52.3	8572.0±77.1

Table6. Elements concentration in sand samples (µg/g) = (mg/Kg) = (ppm)

Sample No.	10	11	12
Element	Mean Concentration±SD		
Au	0.02±0.001	0.02±0.001	0.01±0.001
Cd	0.02±0.001	0.02±0.001	0.02±0.001
Co	0.05±0.002	0.05±0.002	0.05±0.002
Pb	0.09±.004	0.09±.004	0.06±.003
Cu	0.1±0.004	0.1±0.004	0.4±0.001
Ni	0.4±0.02	0.4±0.02	0.5±0.002
Zn	2.3±0.07	2.3±0.07	0.8±0.0003
As	5.0±0.2	5.0±0.2	3.9±0.1
Cr	6.9±0.1	6.9±0.1	4.9±0.2
Mn	9.2±0.3	9.2±0.3	10.7±0.3
Ti	11.9±0.3	11.9±0.3	11.5±0.3
Si	43.9±0.9	44.3±0.9	44.2±0.4
V	60.0±1.1	60.0±1.1	50.6±0.6
P	65.5±1.3	65.5±1.3	92.0±1.3
K	156.2±5.0	75.5±3.0	101.1±1.5
Na	160.0±2.2	156.2±5.0	139.8±1.5
Fe	231.9±3.0	160.0±2.2	160.9±3.5
Al	245.7±3.4	245.7±3.4	245.1±5.0
Mg	264.0±2.1	264.0±2.1	275.2±6.3
S	611.4±9.2	611.4±9.2	436.8±11.8
Ca	7848.3±117.7	7848.3±117.7	7721.8±77.2

Table 7. Elements concentration in sand samples (µg/g) = (mg/Kg) = (ppm)

Sample No.	13	14	15
Element	Mean Concentration±SD		
Au	0.01±0.0005	0.02±0.0005	0.03±0.001
Cd	0.02±0.001	0.02±0.001	0.04±0.02
Co	0.05±0.002	0.05±0.002	0.07±0.003
Pb	0.06±.002	0.06±.003	0.1±.005
Cu	0.4±0.01	0.2±0.008	0.2±0.007
Ni	0.4±0.01	0.4±0.01	2.2±0.08
Zn	0.7±0.0003	0.8±0.0004	3.6±0.08
As	4.0±0.1	3.7±0.04	6.0±0.1
Cr	4.4±0.2	5.5±0.1	6.1±0.2
Mn	9.3±0.3	10.9±0.2	9.9±0.3
Ti	12.1±0.3	11.9±0.4	15.6±0.3
Si	43.8±1.0	44.6±1.0	43.7±1.0
V	56.4±1.2	46.6±1.0	50.9±0.9
P	96.4±3.0	63.6±1.9	83.7±1.6
K	98.1±1.8	93.2±1.1	99.0±1.0
Na	118.8±2.3	100.4±2.0	101.7±0.8
Fe	157.7±4.3	142.1±3.0	175.6±1.9
Al	233.4±2.6	152.5±2.0	221.3±2.0
Mg	257.4±5.9	204.9±3.1	231.6±2.8
S	514.0±13.9	220.8±1.8	432.1±6.0
Ca	7007.7±70.0	7289.2±72.9	9798.1±98.0

Table 8. Elements concentration in sand samples (µg/g) = (mg/Kg) = (ppm)

Sample No.	16	17	18
Element	Mean Concentration±SD		
Au	0.03±0.001	0.03±0.001	0.02±0.001
Cd	0.03±0.001	0.05±0.002	0.04±0.002
Co	0.2±0.006	0.1±0.004	0.07±0.003
Pb	0.2±0.008	0.2±0.008	0.1±0.004
Cu	1.5±0.05	1.4±0.06	0.5±0.02

Table 8. contd.

Ni	1.7±0.05	1.4±0.06	1.0±0.05
Zn	2.2±0.05	2.5±0.07	1.6±0.05
As	4.9±0.1	4.4±0.1	3.6±0.09
Cr	6.7±0.2	7.1±0.2	5.4±0.2
Mn	17.6±0.6	9.9±0.4	6.5±0.2
Ti	40.6±1.3	22.1±0.6	17.9±0.5
Si	42.8±0.4	44.9±0.8	43.9±1.0
V	97.9±1.8	59.8±1.9	61.6±1.8
P	106.5±3.1	115.4±2.9	90.4±2.0
K	122.4±3.4	126.8±3.4	104.5±2.9
Na	171.4±3.4	142.2±3.0	108.7±2.9
Fe	605.8±7.3	422.2±12.2	117.6±2.5
Al	880.8±9.7	434.3±5.6	323.9±5.2
Mg	919.2±10.1	443.7±5.3	353.3±6.7
S	3154.3±31.5	1014.2±10.1	1449.1±17.4
Ca	11508.3±103.6	13691.7±150.6	11775.4±212.

Table 9. Elements concentration in sand samples (µg/g) = (mg/Kg) = (ppm)

Sample No.	19	20	21
Element	Mean Concentration±SD		
Au	0.02±0.001	0.02±0.001	0.04±0.002
Cd	0.02±0.001	0.03±0.001	0.02±0.001
Co	0.1±0.004	0.1±0.004	0.04±0.002
Pb	0.1±0.04	0.2±0.009	0.08±0.004
Cu	1.2±0.04	0.8±0.03	0.1±0.004
Ni	1.4±0.05	1.2±0.05	0.6±0.02
Zn	3.4±0.1	1.3±0.05	1.1±0.04
As	5.1±0.1	4.0±0.1	1.5±0.05
Cr	13.0±0.4	5.3±0.2	3.6±0.1
Mn	14.8±0.3	13.3±0.4	5.3±0.2
Ti	26.7±0.7	30.0±0.8	8.1±0.2
Si	44.5±1.6	43.8±0.6	18.2±0.5
V	68.1±1.6	79.8±2.0	44.0±0.7

Table 9. contd.

P	85.4±1.7	94.9±2.7	69.3±2.1
K	154.9±5.1	144.8±3.5	88.1±1.5
Na	194.6±3.1	188.9±4.0	109.8±1.1
Fe	486.4±6.3	585.6±9.4	184.0±5.7
Al	490.7±10.3	613.8±6.3	310.2±5.9
Mg	535.0±6.4	693.3±12.5	320.9±6.7
S	3127.0±31.3	1081.2±11.9	320.5±8.3
Ca	9824.9±108.1	11754.8±141.0	1717.0±20.6

Table 10. Elements minimum and maximum concentrations in sand samples compared with allowable values

E.	Min. value	Sample No.	Max. value	Sample No.	Allow. Values (mg/kg)
Au	0.01	6-7-9.-12	0.05	17	No data
Cd	0.006	8	0.06	2	0
Co	0.02	6-9	0.04	16-20	50
Pb	0.04	6-9	0. 14	1	14
Cu	0.01	5	14.8	19	15
Ni	0.4	8-9-10-11-13-14	9.9	15	3
Zn	0.5	5	4. 2	1	16
As	4.6	1	12.3	9	1
Cr	3.4	19	6.9	10-11	120
Mn	3.6	6	13.3	20	No data
Ti	9.2	10-11	40.6	16	No data
Si	42.8	16	44.9	17	35.9%
V	55.1	1	159.3	9	50
P	43.7	5	97.9	16	No data
K	46.6	14	194.6	19	No data
Na	75.5	11	258.2	3	No data
Fe	126.6	9	880.8	16	No data
Al	117.6	18	605.8	16	3.2%
Mg	175.6	15	919.2	16	No data
S	1721	1	13691.7	17	No data
Ca	289.4	5	7534.0	1	No data

4. Conclusion and Recommendations

Sample (16) which was collected from Magra at surface contained the higher number of maximum concentrations elements: Co, Ti, P, Fe, Al and Mg. While Shlwan area sample (9), 40 cm depth, contains the maximum number of low elements concentrations which are: Au, Co, Pb, Ni and Fe, also this sample have the higher pH (9.30) over all samples.

In all samples the elements (Au or Cd) represented the low concentrations except sample (5) which have the element (Cu) with low concentration

In samples (1-3) the maximum concentration element is Ca, while the element S showed high concentrations in the rest of the samples.

The toxic trace elements specially (Ni, Cd and As), have concentrations more than back ground values found in the literature of sandstone, while the rest of the trace elements (Co, Pb, Cu, Zn, and Cr) have been found less than allowed concentrations in literature.

The maximum concentrations of the elements: Pb, Zn, Na, Ca and Cd are found at Al sabla region. On the other hand, the maximum concentrations of the elements: As, and V, are found in Shlwan region, while the maximum concentration of Cr was found in Alaaga region. Magra region contains Au, Si, Ti, P, Al, Fe, Mg, and S maximum concentrations. Cu, Mn, and K maximum concentrations are lie in Althuare, Ni at Jaway, and Co at Magra and Althuare.

A further study can be made out to find percentage of silica in sand of Nafud desert so as to be used in some industrial applications such as glass production.

Acknowledgements

The authors gratefully thank Majmaah University for their financial support. Thanks are also due to the Dean of scientific research. Gratitude is also expressed to Kamal O. Ahmed at King Saud University for providing help and support to complete this work.

References

[1] Eduardo, G., Pieter, V., Sergio, A., Giovannim,V., Manuel, V., Kate, A., Al-Juboury,A.,2013. Provenance and recycling of Arabian Desert sand Earth-Science Reviews 120,pp.1-19.

[2] Tooley, F., 1974. The Handbook of Glass Manufacture. I. Books for Industry Inc, New York, USA; pp. 29–30.

[3] George, W., 1954. The Properties of Glass. Science. 120 pp, 834–840,doi: 10.1126/ science.120.3116.463.

[4] Silverman,A.,1953. A Chemist Looks at Glass. Glass Industry. pp. 428–433.

[5] Sandel, E., 1959. Colorimetric Determination of Trace Metals.InterscicencePublications,New York, pp. 123–150.

[6] Uchida, H., Uchida, T., lida, C.,1980. Determination of minor and trace elements in silicate rocks by inductively coupled plasma emission spectrometryAnalyticaChimica Acta116 pp.433–436. doi:10.1016/S0003- 2670(01)95228

[7] Hauptkorn,S.,Krivan,V.,Gercken,B.,Pavel,J.,1997. Determination of trace impurities in high purity quartz by electrochemical vaporization ICP mass Spectrometry using slurry sampling technique. Journal of Analytical Atomic Spectrometry. 2,pp.421–28, doi: 10.1039/a606027g.

[8] Dash,K..,Chandrasekaran,K.,Thangavel,S.,Dha ville, S.,Arunachalam, J., 2004. Determination of trace metallic impurities in high purity quartz by ion chromatography, Journal of ChromatographicaActa, 1022,pp25–31. doi: 10.1016/j.chroma.2, 003.08.014.

[9] Mukherjee,S.,Kundu,D., 2006. Determination of trace impurities in silica sand by inductively coupled plasma atomic emission spectrometry. Transaction of the Indian ceramic Society, 65, pp.169–172.

[10] Voinovitch,A.,Guedon,D., Louvrier, J., 1966. The chemical analysis of silicates. Israel programme for scientific translation Ltd., Jerusalem; pp 250.

[11] Miles, J.,1999. Review papers on analytical methods.Issues and controversy: the measurement of crystalline silica. American Industrial Hygiene Association Journal, 60,pp 396–400.

[12] Verma,D.,Shaw,D.,2001.A comparisonof international silica (α-quartz) calibration standards by Fourier transform-infrared spectrophotometry. The Annals of Occupational Hygine, 45,pp. 429–35.

[13] Akhter,S.,Al-Jowder,O.,1997. Heavymetal concentrations in sediments from the coast of Bahrain. International Journal of Environmental Health Research 7,pp 85-93.

[14] Reguigi, N.,Kugera, J.,Ben,K., 2002. Determination of trace elements in Tunisian soil, desert and beach sand using instrumental Neutron Activation Analysis Proceedings of International Symposium on Environmental Pollution Control and Waste Management pp.70-82, Tunis (EPCOWM'2002).

[15] Bam,P., Akiti, T., Osae, D., Ganyaglo, Y., Gibrilla, A.,2011. Multivariate cluster analysis of some major and trace elements distribution in an unsaturated zone profile, Densu river basin, Ghana. African Journal of Environmental Science and Technology Vol. 5(3), pp. 155-167.

[16] Ushie, F.,Esu,E.,Udom,G., 2005.A Preliminary Evaluation of Otamiri River Sands for the Production of Plain Glass. Journal of Applied Sciences and Environmental Management 9(1),pp 65 – 68.

[17] Hamzah,Z., Ahmad,N., Saat,A.,2009. Determination of Heavy Minerals in Amang from Gajah Ex-Mining Area. The Malaysian Journal of Analytical Sciences, 13, (2),194 – 203.

[18] Mahmoud, H., Abdel-Lateef, A., Attiah, M., 2013. Distribution of Some Elements in the Egyptian Black Sands from Abu Khashaba Beach Area .Journal of Analytical Sciences, Methods and Instrumentation, 3,pp. 62-66.

[19] Morrison,J.,Goldhaber, M.,Holloway,J.,and Smith,D., 2008. Major- and Trace- Element Concentrations in Soils from Northern California: Results from the Geochemical Landscapes Project Pilot Study: U.S. Geological Survey Open-File Report, p,7,pp.1306.

[20] Voica,C.,Dehaelean A.,Iordache,A., and Geana,I., 2012.Method Validation for Determination of Metals in Soils by ICP-MS. Romanian Reports in Physics, 64(1), 221–231.

[21] Haluschak P., Mills G., 1998. Status of Selected Trace Elements in Agricultural Soils of Southern Manitoba Technical Bulletin -6E, A54-8/1998, ISBN 0-662-27098-3.Technical Report 1998-6E Land Resource Unit, Brandon Research Centre, Research Branch, Agriculture and Agri-Food Canada.

[22] Suleman,N.Mohammad,I., Almesned,S. Aljaghwani,A., 2012. Measurements of Some Trace Elements in Street Dust in Zilfi Province at Saudi Arabia Using Inductively Coupled Plasma-Mass Spectrometer World Environment, 2(6), pp.135-139.

[23] Suleman,N.,Mohammad,I.,Almesned,S. Aljaghwani, A.2013. Some Trace Elements in Zilfi Streets Dust. American Journal of Chemistry 3(1),pp 10-13 DOI: 10.5923/j.chemistry.20130301.03